Pergamon

Int. J. Solids Structures Vol. 35, Nos 26–27, pp. 3497–3517, 1998
© 1998 Elsevier Science Ltd
All rights reserved. Printed in Great Britain
0020-7683/98 $19.00 + .00

PII: S0020-7683(97)00213-8

A THREE-DIMENSIONAL VISCOELASTIC CONSTITUTIVE MODEL FOR PARTICULATE COMPOSITES WITH GROWING DAMAGE AND ITS EXPERIMENTAL VALIDATION

K. HA† and R. A. SCHAPERY*

Department of Aerospace Engineering and Engineering Mechanics, The University of Texas at Austin, Austin, Texas 78712, U.S.A.

(*Received* 12 *December* 1996; *in revised form* 21 *July* 1997)

Abstract—A relatively simple nonlinear viscoelastic constitutive model for particle-filled rubber under three-dimensional stress states is developed from an existing axisymmetric constitutive equation and then experimentally verified. In extending the existing model to three dimensions, it is assumed that the damage leads to transverse isotropy with the axis of isotropy coinciding with the local, instantaneous maximum principal stress direction for monotonic loading. Rate-type evolution laws are used to account for the time-dependent changes in damage, and viscoelasticity of the rubber matrix is explicitly taken into account by using so-called pseudo variables; although strains may be large, in this theory rotations must be small. The model has been implemented in a finite element analysis to account for various geometry and loading conditions. Experiments were used to check the model. Various biaxial specimens of different aspect ratios, with and without holes or cracks, were tested with different cross-head rates. Load-deformation information reveal good agreement between theory and experiments, which is far better than using linear theory. A computer code based on the digital image correlation method has been developed and refined for accurate experimental displacement data extraction. The displacement field was further processed with a smoothing program for noise reduction. The specimen surface strain distribution is compared to predictions from theory. Nonlinear theory shows better agreement with experimental strain fields than linear theory. © 1998 Elsevier Science Ltd. All rights reserved.

1. INTRODUCTION

The nonlinear behavior of filled rubber, such as that used for solid propellant, tires and numerous other commercial rubber products, has been studied extensively over many years. Solid propellant, the type of composite investigated in this paper, commonly consists of a soft rubber matrix which is highly filled with hard particles of varying sizes (typically 10–200 microns). The material used in the research was provided by the Naval Weapons Center, and is an inert solid propellant with 70% volume of aluminum, potassium sulfate, and ammonium sulfate embedded in a lightly-crosslinked HTPB (Hydroxyl-Terminated Poly-Butadiene) rubber binder; it was specially compounded to closely simulate the non-linear behavior of a live propellant. The size of particles ranges from 20–200 microns.

The mechanical behavior of propellant is complicated due to the effects of damage growth, viscoelasticity, as well as the possibility of anisotropy and chemical aging. Even when there are small overall strains, they cause non-linear behavior due to large local stress concentrations in the matrix which, in turn, lead to microcracks. That microcracks initiate and grow in filled rubber under mechanical loading is relatively well established; for example Farris (1968), Farris *et al.* (1971) observed specimen dilatation that comes from crack or vacuole formation between the matrix and particles or in the matrix. The amount of dilatation depends not only on the amount of straining, but also on the type of multiaxial loading (axiality), loading rate and temperature.

The problem of developing a realistic mathematical model of the mechanical behavior of highly filled rubber is a difficult one, especially for three- dimensional constitutive relations that can be implemented in a structural analysis using, for example, a finite element code. Superimposed pressure effect (Davis, 1994; Farris, 1968), nonlinear viscoelastic

† Now at CAE Group, Tech. Div., Samsung Display Devices Co., Ltd, 575 Shin-Dong, Seewon City, Korea.
* Author to whom correspondence should be addressed.

response (Farris *et al.*, 1975; Gazonas, 1993), chemical aging (Davis, 1995; Zhou, 1993), micromechanics (Schapery, 1974, 1986, 1991), thermal-mechanical interaction (Hufferd, 1980), the Mullin's effect (Mullins, 1969), and a multiple integral approach (Lai and Findley, 1973), have all been used in the establishment of constitutive models to account for complex behavior of filled rubber composite.

For development of constitutive models for solid propellant, see Farris *et al.* (1975), Simo (1987), Peng (1993a, b), Swanson and Christensen (1983), Schapery (1982, 1987, 1991), Park and Schapery (1997) and Özüpek and Becker (1992). Schapery (1987, 1991) developed a multiaxial nonlinear damage model based on thermodynamics and work potential theory for deformation behavior of particle-filled rubber. This model, which is based on nonequilibrium thermodynamics with internal state variables, was developed to accommodate general three-dimensional loading conditions and then was compared to propellant behavior without significant viscoelastic effects. Recently, a specific constitutive model, which includes the effect of viscoelasticity and time dependent changes in microstructure (such as microcracking) on overall stress–strain behavior, was developed and experimentally verified on inert solid propellant under axial straining and pressure by Park and Schapery (1997). The study included the effect of strain rate, pressure and temperature on the mechanical behavior. The particulate composite with damage was modeled as a homogenized, transversely isotropic continuum.

Although the nonlinear viscoelastic behavior of solid propellant has been recognized for many years, only recently has a structural analysis become computationally practical. Springfield *et al.* (1993) have evaluated the utility of Peng's constitutive law in the ABAQUS (Hibbit *et al.*, 1992) finite element code; it was successful up to 6% strain level in obtaining a convergent solution for a series of Jet Propulsion Laboratory biaxial tests. Simo (1987) used his model in a two-dimensional finite element analysis for a rectangular strip in plane strain clamped on both ends, but the results were not verified by experiments. Laheru (1995) used a piecewise-in-time linear elastic model to approximate nonlinear viscoelastic behavior. He assumed the nonlinear viscoelastic behavior of the propellant is due to the irreversible load-induced microstructural damage accumulation, and a damage measure was defined by the so-called Lebesgue norm of an increasing stress or strain function. Also, the instantaneous secant modulus and effective Poisson's ratio were defined from the combined uniaxial and equal-biaxial data for each linear elastic problem with the time variable frozen; but the effect of the damage orientation was not taken into consideration. Collingwood *et al.* (1995) evaluated nonlinear cumulative damage constitutive theories for solid propellant, such as those of Özüpek, Swanson and Laheru and hyperelastic models such as those of Mooney, Rivlin, Ogden and Peng; most allow for large deformations. They used nonlinear viscoelastic analysis in the finite element analyses of analog wedge, biaxial rail, and equal-biaxial specimens. Also, they conducted tests of two subscale motors to validate the most promising approaches in a motor-like analog.

The objective of this paper is to extend Park and Schapery's (1997) constitutive model for axisymmetric deformation to a general three-dimensional state and assess its validity using reaction loads and local strain distributions in thin and thick plates, with and without holes or cracks, subjected to different strain rates. The viscoelastic constitutive equation is relatively simple and, in contrast to other available equations, permits the use of elastic analysis by means of an easily applied correspondence principle (Schapery, 1984). The theory is limited to small rotations but not to small strains.

2. CONSTITUTIVE MODEL FOR GENERAL THREE-DIMENSIONAL LOADING

In developing the multiaxial constitutive theory from the model for axisymmetric deformation, Schapery's (1991) work potential theory, combined with his micromechanical model, is used as a guide. For a viscoelastic material with general three-dimensional loading and with growing damage, we can always obtain three principal stresses and their directions. One basic assumption is that, with distributed damage, the composite body is locally transversely isotropic with the axis of symmetry oriented in the current local maximum principal stress direction, as suggested by Schapery (1991). We also assume the composite

is isotropic in the absence of damage. It is further assumed that the composite is linearly elastic or viscoelastic for a fixed amount of damage. For an elastic composite with this type of oriented damage, the principal axes of stress and strain are aligned. The elastic strain energy density for transversely isotropic materials can always be written in the form (Schapery, 1986),

$$W = \tfrac{1}{2}(A_{11}e_V^2 + A_{22}e_3^2 + 2A_{12}e_3e_V + A_{44}(\gamma_{13}^2 + \gamma_{23}^2) + A_{66}(\gamma_{12}^2 + e_2^2)) \tag{1}$$

where x_3 is the axis of material symmetry and, in terms of the strain tensor ε_{ij},

$$e_2 \equiv \varepsilon_{22} - \varepsilon_{11}, \quad e_3 \equiv \varepsilon_{33} - e_V/3, \quad e_V \equiv \varepsilon_{11} + \varepsilon_{22} + \varepsilon_{33}$$
$$\gamma_{12} \equiv 2\varepsilon_{12}, \quad \gamma_{23} \equiv 2\varepsilon_{23}, \quad \gamma_{13} \equiv 2\varepsilon_{13}.$$

The five coefficients A_{ij} are the elastic moduli which depend upon the state of damage. Inasmuch as x_3 is the maximum principal strain or stress direction, W in (1) is reduced to W' (say) in terms of principal strains; thus, with $\gamma_{13} = \gamma_{23} = \gamma_{12} = 0$,

$$W' = \tfrac{1}{2}(A_{11}e_V^2 + A_{22}e_3^2 + 2A_{12}e_3e_V + A_{66}e_2^2) \tag{2}$$

which is seen to be independent of A_{44}. The stress–strain equations may be expressed for principal stresses by taking principal strains $\varepsilon_1 \equiv \varepsilon_{11}$, $\varepsilon_2 \equiv \varepsilon_{22}$, $\varepsilon_3 \equiv \varepsilon_{33}$ as independent variables. Thus,

$$\sigma_i = \frac{\partial W'}{\partial \varepsilon_i} \quad (i = 1, 2, 3). \tag{3}$$

Explicitly, the principal stresses are,

$$\begin{aligned}
\sigma_1 &= (A_{11} - \tfrac{1}{3}A_{12})e_V + (A_{12} - \tfrac{1}{3}A_{22})e_3 + A_{66}e_2 \\
\sigma_2 &= (A_{11} - \tfrac{1}{3}A_{12})e_V + (A_{12} - \tfrac{1}{3}A_{22})e_3 - A_{66}e_2 \\
\sigma_3 &= (A_{11} + \tfrac{2}{3}A_{12})e_V + (A_{12} + \tfrac{2}{3}A_{22})e_3.
\end{aligned} \tag{4}$$

In general, the axis of isotropy will not be parallel to an axis in the global coordinate system used to represent the local strains in a structural analysis. In order to allow for an arbitrary orientation, write

$$\mathrm{d}u_i' = \varepsilon_i \, \mathrm{d}x_i' \quad \text{(no sum on } i\text{)} \tag{5}$$

where ε_i are the principal strains (assumed small for now) referred to principal strain directions, x_i'. The relationship between the strains ε_{pq} the global reference coordinate system and local material coordinates is given by the usual second-order tensor transformation law,

$$\varepsilon_i = m_{ip}m_{iq}\varepsilon_{pq} \quad (p, q = 1, 2, 3\,; \text{no sum on } i) \tag{6}$$

where m_{ij} is the cosine of the angle between x_i' and x_j axes. Substitution of ε_i from (6) into (2) leads to W' in terms of ε_{pq}.

The previously developed constitutive model (Park and Schapery, 1997), using the same inert propellant as here, for uniaxial specimens under axial strain ε and confining pressure p is adopted here and modified as necessary. Details of the characterization process are given elsewhere (Park, 1994), including a refinement of the method of identifying the

Table 1. Analytical expressions for the material functions (primary units are pounds, inches, seconds)

$$C_{11}(S_1) = 2310 - 869 \cdot S_1^{1/5} + 1679 \cdot S_1^{2/5} - 2000 \cdot S_1^{3/5} + 561 \cdot S_1^{4/5}$$
$$C_{12}(S_1) = 0.0744 \cdot S_1^{1/2} + 0.0333 \cdot S_1 - 0.00248 \cdot S_1^{3/2}$$
$$C_{22}(S_1) = -1.705 \cdot 10^{-5} \cdot S_1^{1/2} - 1.544 \cdot 10^{-5} \cdot S_1 - 1.109 \cdot 10^{-5} \cdot S_1^{3/2}$$
$$C(S_2) = 1 + 0.0925 \cdot S_2^{1/5} - 0.373 \cdot S_2^{2/5} + 0.07405 \cdot S_2^{3/5}$$

material parameters (Park *et al.*, 1996). For the moment, let us give the elastic version of this model with damage; extension to a viscoelastic body will be given later:

Dual Energy Density Function:

$$W_D = C_{11}(S_1)C(S_2)\frac{\varepsilon^2}{2} + C_{12}(S_1)\varepsilon p + \frac{1}{2}C_{22}(S_1)p^2. \tag{7}$$

Stress–Strain Relations:

$$\sigma \equiv \frac{\partial W_D}{\partial \varepsilon} = C_{11}(S_1)C(S_2)\varepsilon + C_{12}(S_1)p$$
$$e_V = \frac{\partial W_D}{\partial p} = C_{12}(S_1)\varepsilon + C_{22}(S_1)p. \tag{8}$$

Internal State Evolution Law:

$$\dot{S}_m = \left(-\frac{\partial W_D}{\partial S_m}\right)^{\alpha_m} \quad (m = 1, 2) \tag{9}$$

where α_m's are constants and the overdot denotes a time derivative. The two internal state variable (ISVs) S_1 and S_2 account for changes in internal structure, such as microcracking and disentanglement of polymer chains (which we call "damage").

In order to determine A_{ij} in (2) in terms of previously determined material functions C_{ij}'s (8) can be used to obtain stress–strain relationships in the form in (4). A comparison of (4) and (8) leads to the A_{ij}'s in terms of C_{ij}'s, except for A_{66},

$$A_{11} = \frac{1}{9}\left(\hat{C}_{11} - \frac{(C_{12} - 3)^2}{C_{22}}\right),$$
$$A_{12} = \frac{\hat{C}_{11}}{3} + \frac{C_{12}}{C_{22}}\left(1 - \frac{C_{12}}{3}\right), \quad A_{22} = \hat{C}_{11} - \frac{C_{12}^2}{C_{22}} \tag{10}$$

in which

$$\hat{C}_{11} \equiv C_{11}C. \tag{11}$$

Here $C_{ij}(S_1)$ $(i,j = 1,2)$ and $C(S_2)$ are material functions determined from the characterization processes for the case of a specimen under axial strain ε and pressure p. A summary of the material functions is in Table 1. It is noted that some constants in the material functions in the table were slightly modified from those in Park's original equations. A 7% error in the cross-sectional area measurement and aging due to the time gap of a few years between the two sets of tests are believed to be the sources of the difference (Ha,

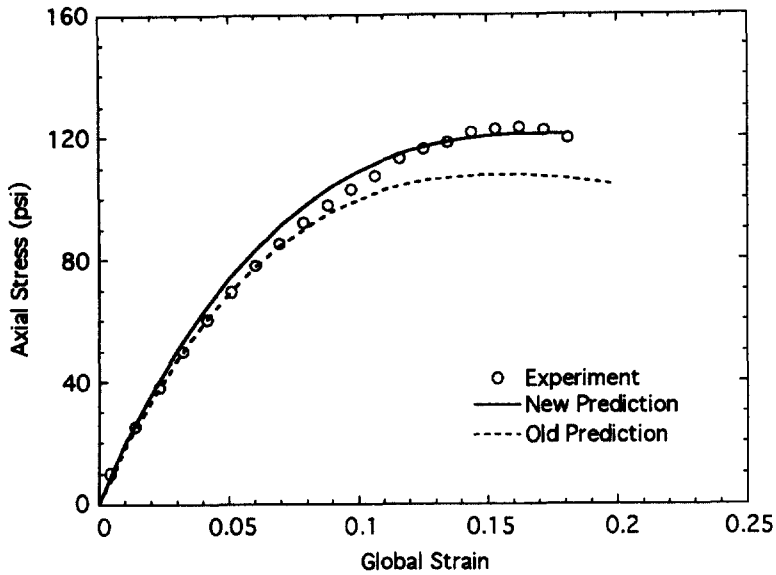

(a) $\dot{\varepsilon} = 0.36\ \text{min.}^{-1}$

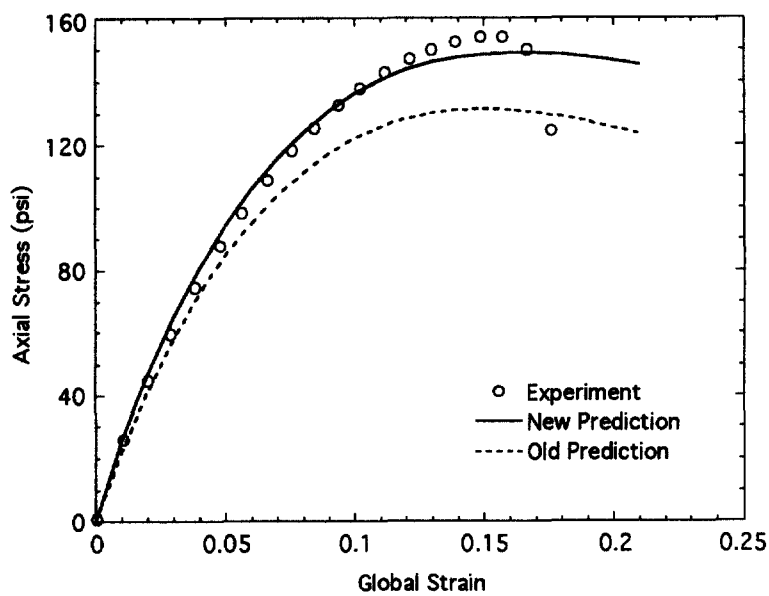

(b) $\dot{\varepsilon} = 3.6\ \text{min.}^{-1}$

Fig. 1. Predictions and experimental results for uniaxial tests.

1996). Figure 1 gives the comparison between stress–strain curves of uniaxial tension tests and predictions of the previous constitutive equations and modified equations for two different strain rates. It may be observed that the previous constitutive equations predict about 15% lower maximum stress than the new experimental values. The average of at least three specimens per condition is shown.

The shear modulus A_{66} used in (2) was found by Schapery (1991) from a micro-mechanical model to be relatively insensitive to microcracking, the thus we shall use the

shear modulus in the undamaged state. Since the undamaged material can be regarded as an incompressible isotropic material,

$$A_{66} = G_{\text{init}} = \frac{E_{\text{init}}}{2(1+\nu_{\text{init}})} \cong \frac{E_{\text{init}}}{3}. \tag{12}$$

As further support for (12), we have checked for possible sensitivity of the reaction load to A_{66} in the three-dimensional analysis. Using 90% of the A_{66} in (12), a specimen without a hole or a crack was analyzed using finite element analysis. The peak load changed by only 0.3% with this 10% reduction in A_{66}.

To accommodate viscoelasticity of the matrix, and thermorheological simplicity in its temperature dependence, the extension to viscoelasticity is accomplished by replacing the strains ε_{ij} in an elastic formulation with pseudo strains ε_{ij}^R defined by,

$$\varepsilon_{ij}^R = \frac{1}{E_R}\int_0^{\xi} E(\xi-\xi')\frac{\partial \varepsilon_{ij}}{\partial \xi'}\mathrm{d}\xi'. \tag{13}$$

Here $E(\xi)$ is relaxation modulus, E_R is termed reference modulus which is a free constant with the same dimension as the relaxation modulus, ξ is the so-called reduced time and is defined as

$$\xi = \int_0^t \frac{\mathrm{d}t'}{a_T} \tag{14}$$

and $a_T = a_T(T)$ is a material function of temperature. This replacement with pseudo strains was justified by Schapery (1981) with and without growing damage. The resulting constitutive equations and internal state evolution laws for the viscoelastic model under general three-dimensional loading are like those given above, but notation for principal pseudo strains is used:

Pseudo Strain Density Energy Function:

$$W^R = \tfrac{1}{2}[A_{11}(S_1,S_2)(e_V^R)^2 + A_{22}(S_1,S_2)(e_3^R)^2 + 2A_{12}(S_1,S_2)e_3^R e_V^R + A_{66}(e_2^R)^2] \tag{15}$$

where $e_2^R = \varepsilon_2^R - \varepsilon_1^R$, $e_3^R = \varepsilon_3^R - e_V^R/3$ and $e_V^R = \varepsilon_1^R + \varepsilon_2^R + \varepsilon_3^R$.

Stress–Strain Relations:

$$\begin{aligned}
\sigma_1 &= (A_{11} - \tfrac{1}{3}A_{12})e_V^R + (A_{12} - \tfrac{1}{3}A_{22})e_3^R + A_{66}e_2^R \\
\sigma_2 &= (A_{11} - \tfrac{1}{3}A_{12})e_V^R + (A_{12} - \tfrac{1}{3}A_{22})e_3^R - A_{66}e_2^R \\
\sigma_3 &= (A_{11} + \tfrac{2}{3}A_{12})e_V^R + (A_{12} + \tfrac{2}{3}A_{22})e_3^R.
\end{aligned} \tag{16}$$

Internal State Evolution Law:

$$\frac{\partial S_m}{\partial \xi} = \left(-\frac{\partial W^R}{\partial S_m}\right)^{\alpha_m} \quad (m = 1, 2) \tag{17}$$

where $\alpha_1 = 6$ and $\alpha_2 = 4.5$ for our material.

Thermal expansion may be easily included (Schapery, 1981). Here, we observe only that if it is independent of temperature history, then one replaces the principal strains ε_i inside the convolution integral (13) by $\varepsilon_i - \alpha_i \Delta T$, where ΔT is the temperature change and the α_i are the expansion coefficients; $\alpha_1 = \alpha_2$ with transverse isotropy.

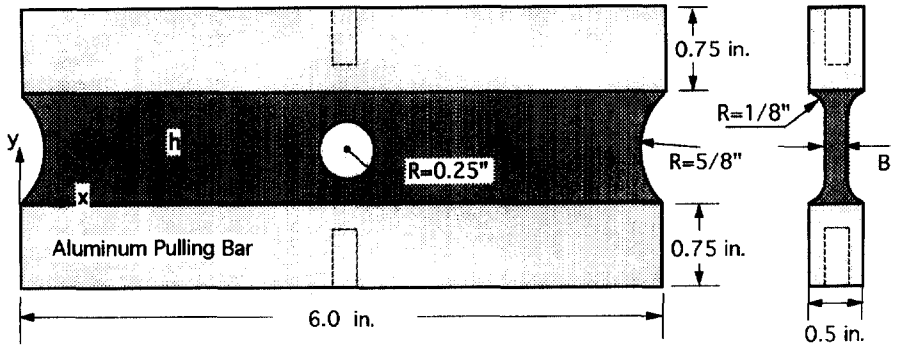

Fig. 2. A biaxial strip specimen with a central hole.

3. LABORATORY EXPERIMENTS AND MODEL IMPLEMENTATION

3.1. *Test program*

The plate specimens employed were so-called biaxial strips. They were rectangular in shape and bonded to relatively rigid aluminum grips on the upper and lower surfaces, as illustrated in Fig. 2; note that an (x, y, z) global coordinate system (rather than x_i) is now used. The specimens were cut from large, cast blocks; all specimen surfaces were machined smooth. Some of our biaxial specimens were unflawed while others contained manufactured defects, namely a centered circular hole or a centered through-crack. The thickness of some of our biaxial specimens varied near the top and bottom bondlines resulting in an "I-shape", as shown in the figure; unless noted otherwise, a constant thickness geometry is used in the discussion in Section 4. The specimens were loaded in tension in an Instron machine. Preliminary tests of biaxial specimens without the illustrated circular end cut-outs or without an I-shape thickness revealed premature failure near the bondline between the specimen and a grip due to the high stress concentrations. All specimens were tested in the ambient laboratory environment for which $a_T = 1$ and $\Delta T = 0$.

Two types of tensile tests, uniaxial tension tests using specimens as described by Park and Schapery (1997) for verification and calibration of the previous constitutive model, and biaxial strip tests were performed; the latter were used for evaluation of the three-dimensional constitutive model. Four specimens were tested under each condition to obtain the results in Fig. 1. Among them, those showing a major deviation from the average curve (usually due to large initial voids or aggregated particles) were discarded. Displacement rates of 1″/min and 10″/min were selected because they correspond to 0.36/min, 3.6/min strain rates, which are located logarithmically at about mid points in the axial strain rates of 0.1″/min, 1″/min and 10″/min used in the biaxial strip tests.

The three-dimensional stressing effect in the biaxial strips was studied by changing the thickness-to-height aspect ratio by using combinations of $h = 0.6$, 1.0″ and $B = 0.2$, 0.25, 0.3″. Specimens of three different aspect ratios were tested, 1 : 2, 1 : 4, 1 : 5, and the results were compared with those of a plane stress condition. The effect of loading rate on the viscoelastic response was also checked with the tests of 0.1″/min, 1″/min and 10″/min cross-head speed. For each strain rate, two biaxial specimens were tested; in a few cases the specimen cracked prematurely, and thus was not used in the comparison of theory and experiment. Table 2 lists the tests.

Biaxial strip specimens with holes or cracks were tested for comparison of experimental and theoretical strain field distributions and reaction forces. A specimen with a hole creates a moderate strain concentration around the perimeter of the hole, while a specimen with a central through-crack provides severe strain concentration around the crack tips, which in turn creates more damage and nonlinear behavior.

A strain analysis was performed on digitized images at 5 and 10% global strain level for specimens with circular holes. The initiation of macrocrack growth occurred at either side of the hole wall at about 11% global strain. Two specimens with a central through-crack were tested under 0.1″/min displacement rate and images recorded at every 2% global

Table 2. Summary of tests results and predictions for reaction load

Test name	Defect shape	$\dot{\varepsilon}$ (/min)	Aspect ratio*	Max. load† (lbs)	% Diff.	Strain (%) at max load†
Test 40	—	0.1	0.2	137.0 (137.8)	+0.6	11.9 (12.6)
Test 42	—	0.1	0.2	136.7 (137.8)	+0.8	12.1 (12.6)
Test 45	—	0.1	0.2	135.4 (137.8)	+1.7	12.7 (12.6)
Test 47	—	0.1	0.2	136.9 (137.8)	+0.6	10.4 (12.6)
Test 48	—	1.0	0.2	160.5 (170.0)	+5.6	12.8 (12.0)
Test 49	—	1.0	0.2	160.5 (170.0)	+5.6	12.0 (12.0)
Test 44	—	10.0	0.2	196.8 (209.9)	+6.2	9.1 (11.1)
Test 50	—	10.0	0.2	205.1 (209.9)	+2.3	10.1 (11.1)
Test 30	—	0.1	0.25	165.5 (173.2)	+4.4	10.3 (11.2)
Test 72	—	1.0	0.5	266.9 (263.8)	−1.2	8.8 (10.3)
Test H1	Hole	0.1	0.25	161.5 (159.5)	−1.2	10.4 (11.0)
Test H2	Hole	0.1	0.25	183.9 (169.7)	−7.7	10.3 (10.9)
Test H3	Hole	0.1	0.25	163.0 (159.5)	−2.1	11.7 (11.0)
Test H4	Hole	0.1	0.25	155.7 (149.5)	−4.0	11.2 (11.0)
Test C10	Crack	0.1	0.25	135.8 (144.2)	+5.8	9.1 (10.8)
Test C11	Crack	0.1	0.25	137.0 (144.2)	+5.0	8.7 (10.8)
Average					+1.7	

* Thickness-to-sheet height aspect ratio.
† Numbers in ( ) represent finite element predictions.

strain increment. Crack growth was initiated somewhere between 6 and 8% global strain. At 8% in the C11 specimen, for example (see Table 2), about 0.13″ total crack extension was measured and 0.39″ measured at a 10% global strain state. Since crack growth had already developed at 8% global strain, the deformed image under 6% global strain was selected for strain analysis and comparison with theory. Note that our prediction did not account for crack growth.

The digital image correlation method (DICM) was used for measuring in-plane horizontal and vertical displacement components, u and v, respectively. Details of the principle and the data reduction scheme of DICM used in this study are given by Ha (1996). The two-dimensional smoothing algorithm used was mainly that of Dohrmann and Busby (1990). The algorithm uses Wahba's (1975) generalized cross validation (GCV) method to determine the level of noise internally. After the smoothing parameter was determined, the smoothed displacement outputs were assumed free of experimental noise. The small strain (displacement gradient) measure was used.

The effects of out-of-plane displacement w and out-of-plane rotations $w_{,x}$ and $w_{,y}$ on the DICM algorithm were assumed negligible, guided by the result from Post *et al.* (1987) for specimens with similar material and geometry. They used the shadow moiré method for w field determination for both $8 \times 2 \times 0.25''$ and $8 \times 2 \times 0.6''$ specimens and found that the influence of w on in-plane strains was significant. Also, in a well-focused optical test set-up, a significant amount of w displacement can be detected from careful monitoring of the test specimen as well as from the test results; the image is blurred by the change in depth-of-field due to out-of-plane displacement, especially for the tests under high lens magnification. On the other hand, for problems where an influence of w is significant, DICM extended for three-dimensional deformation measurement (Kahn-Zetter and Chu, 1990) may be employed. The smoothed displacement used two-dimensional cubic spline functions; the strain outputs were directly available from the smoothed displacement functions.

3.2. *Implementation of the theoretical model*

The solution of the elastic boundary value problem is determined from the iterative procedures discussed in ABAQUS (Hibbit *et al.*, 1993) for any kinematically admissible displacement and strain functions. The implementation of user-defined constitutive relations in the finite element analysis is described in the following steps for sufficiently

small increments in pseudo grip displacement loading; this displacement is calculated from the given physical displacement using an equation like (13):

(1) Starting with a linear elastic isotropic analysis in terms of pseudo variables using a small prescribed pseudo displacement increment, and specifying Young's modulus and a Poisson's ratio slightly less than 0.5, determine the local pseudo strains.
(2) For trial pseudo strain functions, transform the local strains in a reference Cartesian coordinate system (x, y, z) to an orthogonal coordinate system in the local principal stress (or, equivalently, pseudo strain) directions $(1, 2, 3)$ according to (6), and find ε_1^R, ε_2^R and ε_3^R (maximum). Calculate e_V^R, e_2^R, e_3^R and update W^R, which is a function of solution values of S_1 and S_2 that are passed in from the previous incremental analysis.
(3) Evaluate the principal stresses using (16) and transform them back to the stresses in (x, y, z) coordinate system. In the solution procedures in a problem with a user-defined material in ABAQUS, six stress components and the thirty six components of incremental stiffness matrix, $\tilde{C}_{ij} \equiv (\partial\sigma_j/\partial\varepsilon_i^R)$ $(i, j = 1, 2, \ldots, 6)$ referred to (x, y, z) coordinate system, should be provided for outputs from the user-subroutine. In our analysis, $\tilde{C}_{ij}$ was calculated based on constant S_i to obtain a simple expression; in ABAQUS, the incremental stiffness is mainly used for fast convergence of the solution (Hibbit *et al.*, 1992).
(4) After finding the pseudo displacement functions which satisfy equilibrium equations in a global sense within a small enough tolerance (usually 0.005 lbs), use e_v^R, e_2^R, e_3^R and W^R from step 2 to find local increments of S_1 and S_2 from the damage evolution law (17) and the associated time increment.
(5) Change all the pseudo variables into physical variables using the uniaxial creep compliance. This step is illustrated in the Results and Discussion section.
(6) Increase the loading by an incremental boundary pseudo displacement and solve a new elasticity problem at steps 2 and 3 and proceed to steps 4 and 5.

Note that the linear elastic material properties were selected for the material parameters in step 1. The value of the uniaxial linear relaxation modulus at $t = 1$ s was arbitrarily used for Young's modulus. This is the value adopted for the reference modulus E_R, but a different choice of modulus would not affect the viscoelastic solution. The Poisson's ratio of 0.499 was used in step 1; this value, rather than 0.5, was selected to be able to start the solution without encountering numerical problems and to provide the nearly incompressible behavior exhibited by propellant under small stresses. Numerical difficulties are also encountered if zero damage $(S_1 = S_2 = 0)$ is used in the first increment as this corresponds to incompressible behavior for the given material functions; this problem was avoided in step 1 by arbitrarily using 0.001 for both ISVs.

Finite element models of a specimen with a 0.5″ diameter hole and a specimen with 1″ long center crack are shown in Fig. 3. For most cases, a one-eighth specimen was modeled using the symmetry conditions with respect to the coordinate planes; for a few cases, a one-quarter specimen was modeled for direct construction of surface strain contour maps. For the thickness direction, two layers of elements were usually enough, which is the same as four layers of elements without symmetry about the x–y plane. Some modification from the meshes shown or more refined meshes were made as necessary. Twenty-noded, three-dimensional continuum isoparametric elements with reduced integration were used to model the three-dimensional specimens.

4. RESULTS AND DISCUSSION

4.1. *Load prediction and comparison to experiment*

Figures 4–6 show the reaction load results from the nonlinear analysis for 0.2″ thickness biaxial strip specimens with 0.1″/min, 1″/min and 10″/min cross-head speeds, respectively. In each figure, the solid line reflects the reaction force normalized with thickness predicted from a full-three dimensional finite element analysis with the nonlinear constitutive model. Each graph overlays both experimental results in symbols and predictions along with plane stress and P–e analysis defined below.

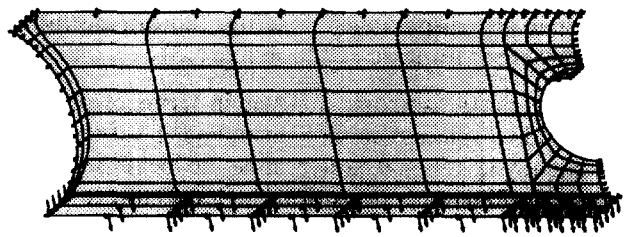

(a) A Quarter Specimen with a Central Hole

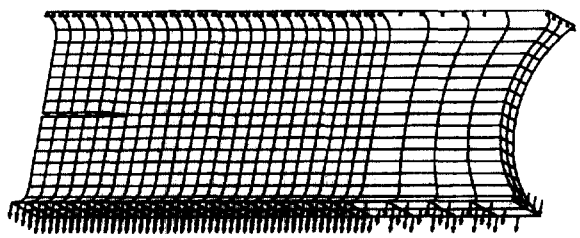

(b) A Quarter Specimen with a Through Crack

Fig. 3. Examples of finite element models used for the biaxial strip specimens.

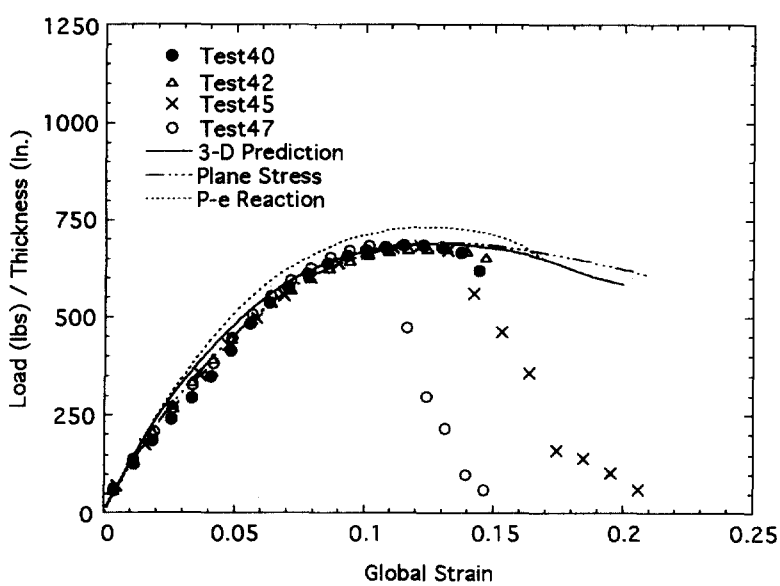

Fig. 4. Reactions for $\dot{\varepsilon} = 0.1\ \text{min}^{-1}$ ($t = 0.2''$, $h = 1.0''$).

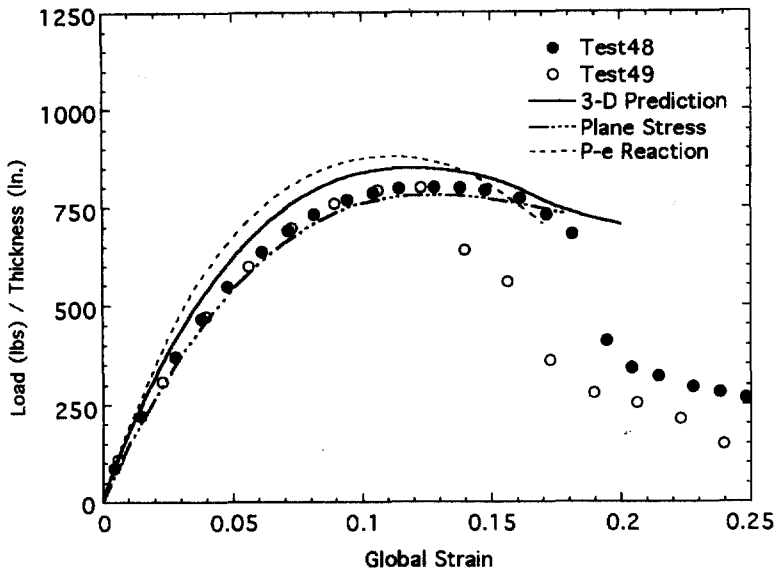

Fig. 5. Reactions for $\dot{\varepsilon} = 1.0\ \text{min}^{-1}$ ($t = 0.2''$, $h = 1.0''$).

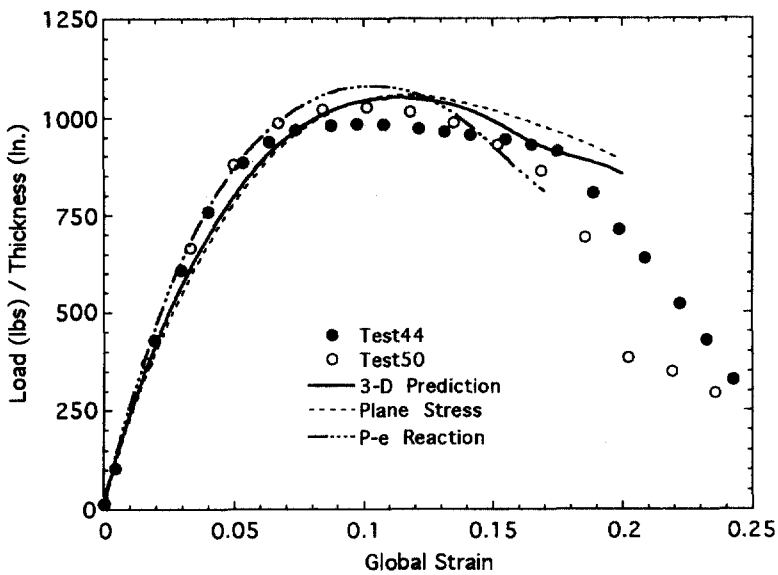

Fig. 6. Reactions for $\dot{\varepsilon} = 10\ \text{min}^{-1}$ ($t = 0.2''$, $h = 1.0''$).

The P–e reaction predictions in the figures were calculated for $R = L_{\text{eff}} R_{P\text{-}e}$, where $R_{P\text{-}e}$ is a reaction of a cross-sectional area under a plane strain condition in the length direction for a specimen of uniform thickness B and unit length. L_{eff} is the effective length; L_{eff} is conveniently defined as $L_{\text{eff}} = R_{\text{linear}}/\sigma_{\text{inf}} B$ where R_{linear} is the reaction load from three-dimensional linear elastic analysis with Poisson's ratio of 0.499 and σ_{inf} is the linear elastic axial stress for the infinitely long, thin strip with the same global strain and Poisson's ratio as those in the three-dimensional analysis. Apparently, except for high strains, the plane stress prediction provides a lower bound to a prediction from three-dimensional nonlinear analysis, while the P–e prediction provides an upper bound; the closeness of the plane stress and three-dimensional predictions is not surprising in view of the low specimen aspect ratio. For zero strain specified in the thickness and length directions, the reaction in the linear elastic analysis with Poisson's ratio of 0.499 is 125 times that of the plane stress case;

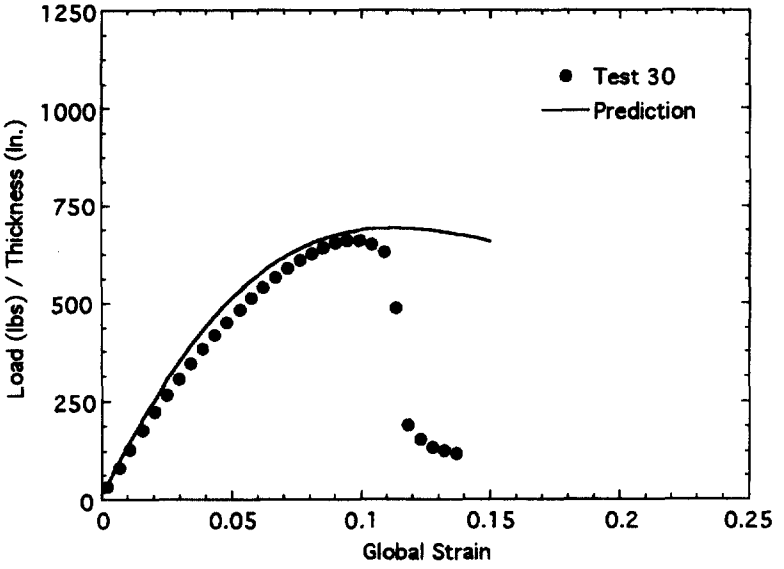

Fig. 7. Reactions for $\dot{\varepsilon} = 0.1\ \text{min}^{-1}$ ($t = 0.25''$ (I-shape), $h = 1.0''$).

with damage, the same trend as in the linear elastic analysis was found in the initial stage of the reaction curve, but the reaction reaches a maximum value at less than 1% global strain due to the high constraint.

The comparison between theoretical predictions and experimental results generally show good agreement. In almost all of the cases, the discrepancies increase after the peak load; but it should be mentioned that those discrepancies are due to specimen failure from strain localization in the form of local macrocracking, which eventually develops into a large macrocrack. For most cases, the macrocrack initiated in the middle of the actual biaxial strip; for a few cases, the crack initiated at one of the specimen's curved ends. Separate macrocracks formed near the initial macrocrack and then interconnected to form a dominant macrocrack. The macrocracks grew steadily and quasi-statically until the specimens were in two pieces.

For all subsequent predictions we used a full three-dimensional finite element analysis, accounting for spatial and timewise damage variations. In Fig. 7, the theoretical prediction is compared to the experimental load-displacement curve for the biaxial strip specimen with "I-shape" varying thickness. Figure 8 reveals the reaction comparison between the prediction and the test for a specimen of uniform thickness with 1 : 2 thickness-to-height aspect ratio. Three-dimensional analysis predicts the experimental load very closely up to the maximum load before a macrocrack grows to produce global failure. Comparing this with the reaction for a 1 : 5 aspect ratio in Fig. 5 for $\dot{\varepsilon} = 1.0\ \text{min}^{-1}$ to see the three-dimensional effect, it is observed that the maximum theoretical and experimental loads in Fig. 8 show only a slight increase, but the experimental strain at maximum load is noticeably smaller in Fig. 8 than in Fig. 5. The closeness of the maximum loads, considering the difference in thickness constraint, is not too surprising because the higher constraint at a given strain produces more damage; as a direct indication of the differences in constraint, it is found that the initial stiffness in Fig. 8 is 1.5 times that in Fig. 5.

The experimental reaction and prediction for a specimen with a center hole are given in Fig. 9; it is noteworthy that the global response is not very sensitive to the hole, as may be seen by comparing Figs 7 and 9. Figure 10 shows the reaction comparison between the nonlinear prediction and test results for biaxial strip specimens with a 1″ long central through-crack. The crack growth initiated at the crack tip at the global applied strain of less than 8%. The comparison is in a good agreement up to the point of crack growth initiation.

The summary in Table 2 shows the percent difference between the tests and predictions for load. Each specimen was tested to failure. A relatively big difference between the

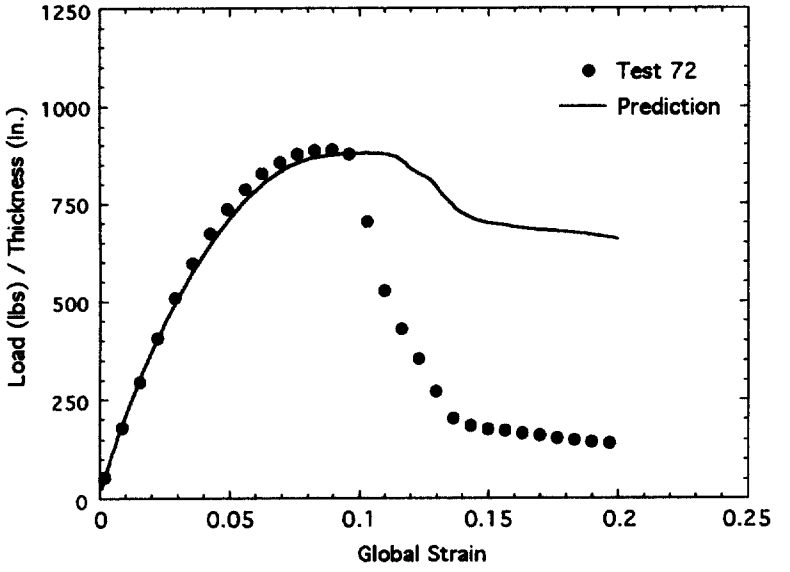

Fig. 8. Reactions for $\dot{\varepsilon} = 1.0\ \text{min}^{-1}$ ($t = 0.3''$, $h = 0.6''$).

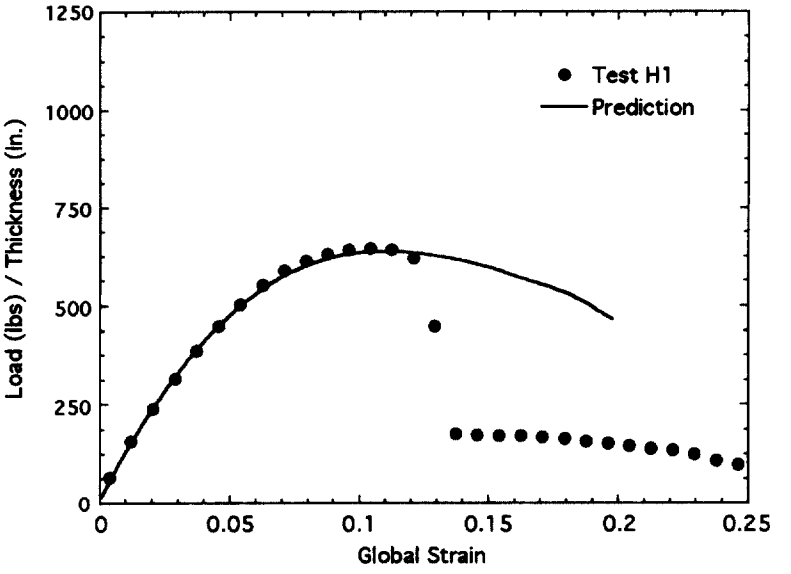

Fig. 9. Reactions for a specimen with a hole ($\dot{\varepsilon} = 0.1\ \text{min}^{-1}$, $t = 0.25''$ (I-Shape), $h = 1.0''$).

predictions and experiments for the strain at the peak load is primarily due to macrocrack growth in the test specimens, which was not accounted for in the theory. It should be added that the agreement between theory and experiment for all load-strain records is far better than achieved by linear viscoelasticity theory; in this latter case, the load is nearly linear in strain, matching the experimental data only at very small strains.

4.2. *Determination of strain and displacement fields*

Local experimental and theoretical strain comparison have been made to check the quality of theoretical strain field predictions, including those outside the strain range of uniaxial tests used for the material characterization. (In the uniaxial test, about 15% was the available maximum axial strain under room temperature and ambient pressure.) The

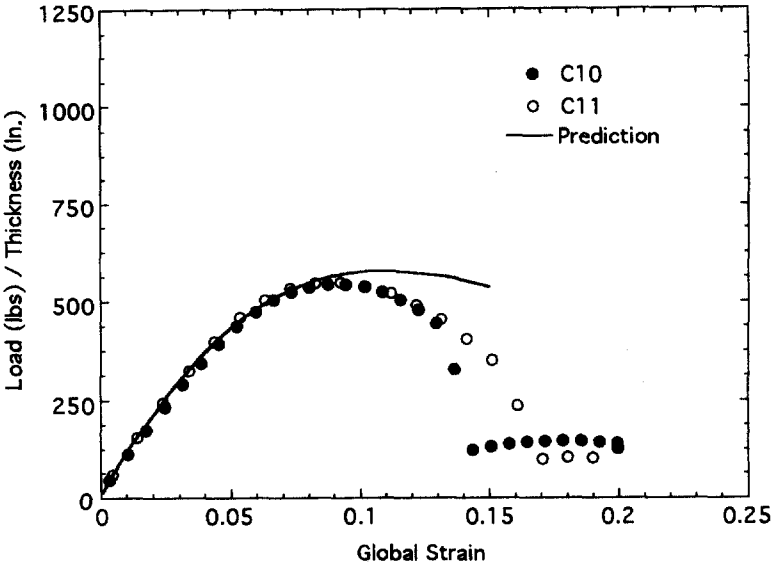

Fig. 10. Reactions for a specimen with a crack ($\dot{\varepsilon} = 0.1\ \text{min}^{-1}$, $t = 0.25''$(I-Shape), $h = 1.0''$).

physical strain calculation can be done numerically from the pseudo strain solution, using a piecewise constant pseudo strain rate approximation and the inverse of (13); e.g. with $a_T = 1$,

$$\varepsilon(t) = E_R \int_0^t D(t-\tau)\frac{\mathrm{d}\varepsilon^R}{\mathrm{d}\tau}\mathrm{d}\tau \tag{18}$$

where $D(t)$ is the creep compliance. It should be added that the quasi-elastic approximation to (18), in which $\varepsilon \simeq E_R\varepsilon^R/E_s(t)$, where E_s is the constant-rate secant modulus, provides quite accurate results (Ha, 1996) for all of our tests.

Numerous tests and analyses have been conducted for obtaining good experimental strain and displacement distributions by calibrating and fine-tuning the experimental methods, including the DICM for strain analysis (Ha, 1996). Theoretically, it was found that the strain distribution from a linear solution under the prescribed displacement boundary condition is often quite close to that from the nonlinear solution of the problem with a nonlinear constitutive equation. (Note also that from dimensional analysis the linear viscoelastic strain distribution is the same as the linear elastic solution if the same displacement boundary condition is prescribed and the Poisson's ratio is constant.) If the local largest principal strain and its direction change during the loading due to nonuniform damage evolution, the linear and nonlinear strain predictions show differences. Also, because the damage doe not evolve much under small local strain, i.e. up to 5% or so, the difference is small, especially for specimens without any manufactured flaw, i.e. a hole or a crack. The subsequent discussion concerns specimens with a precut hole or crack. They all have the I-shaped thickness profile in order to decrease the tendency for premature damage localization close to the bondlines.

Example strain contour maps for 10% global strain are shown in Fig. 11 for a specimen with a circular hole. The experimental strain contours show small local irregularities due to material inhomogeneity. Figure 12 shows contour predictions from the finite element analysis of the nonlinear model for 10% global strain. Both the linear and nonlinear predictions are generally similar in shape except for some differences at the hole perimeter regions; in Figs 11 and 12, the hole center is at (3.0, 0.5) in the maps. The closer to the hole, the discrepancies between linear and nonlinear analyses grow bigger. The nonlinear model creates damage due to high strain concentrations near the hole. The maximum principal strain becomes bigger from material softening due to damage growth; also, the

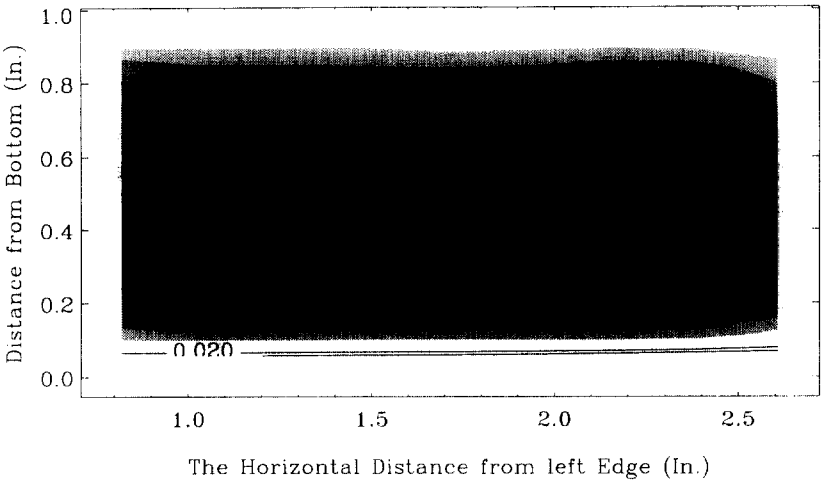

Fig. 11. Experimental contour map of ε_y (10% global strain).

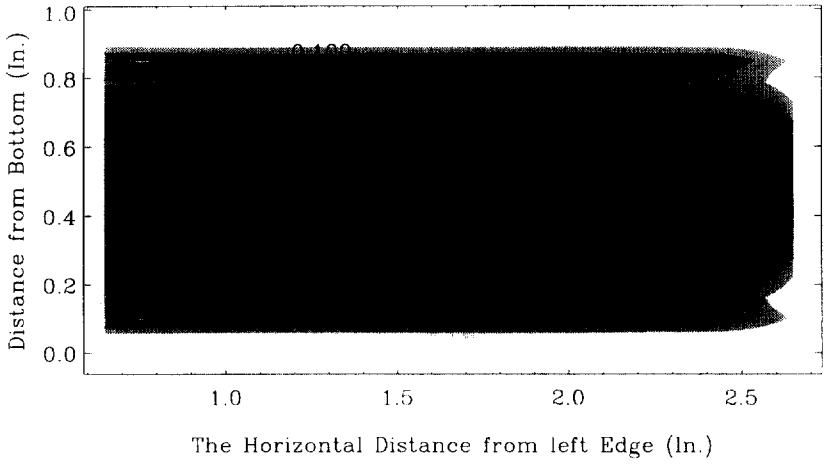

Fig. 12. Theoretical prediction of ε_y (10% global strain).

local axis of material symmetry changes due to rotation of the maximum principal strain direction. By and large, the nonlinear prediction lines match closely those from experiments, though the theory is smoother and simpler in shape than those from experiments. Several additional strain and displacement results are compared in Ha's study (1996).

It is informative to construct a section cut on the surface contour map for more direct comparison. Horizontal displacement along a horizontal line and vertical strain along a vertical line are used for the section plot comparison in Figs 13 and 14, respectively. The vertical line cut was made in Figs 11 and 12 at 0.125″ from the hole wall. Figure 13 reveals the horizontal displacement comparison along the mid-height horizontal line for 5% global strain. A vertical strain section plot for 10% global is in Fig. 14. In this figure it is clear the nonlinear model predicts the vertical strain better than the linear analysis; the somewhat irregular strain variation near the top and bottom surfaces is due to the I-shaped thickness variation.

Specimens H3 and H4 were mainly prepared for the study of the close-to-hole strain field, and were intended to replicate the results under the same test environment and conditions. The scanned area was centered at the hole center, and both sides of the specimen from the hole center were used for DICM analysis; four replica sets of strain data were available from experiments. Figure 15 presents section comparisons between predictions and experiment for vertical strain. It should be noted that the section plot comparison is

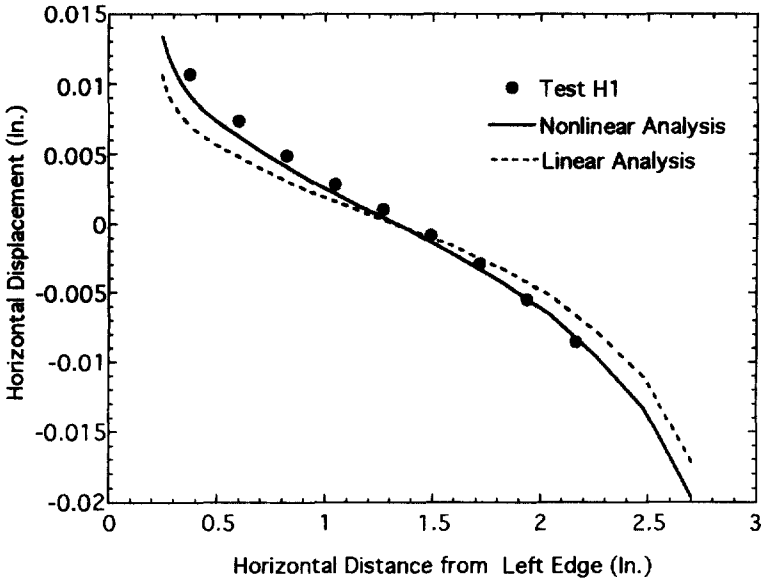

Fig. 13. Horizontal displacement comparison (5% global strain).

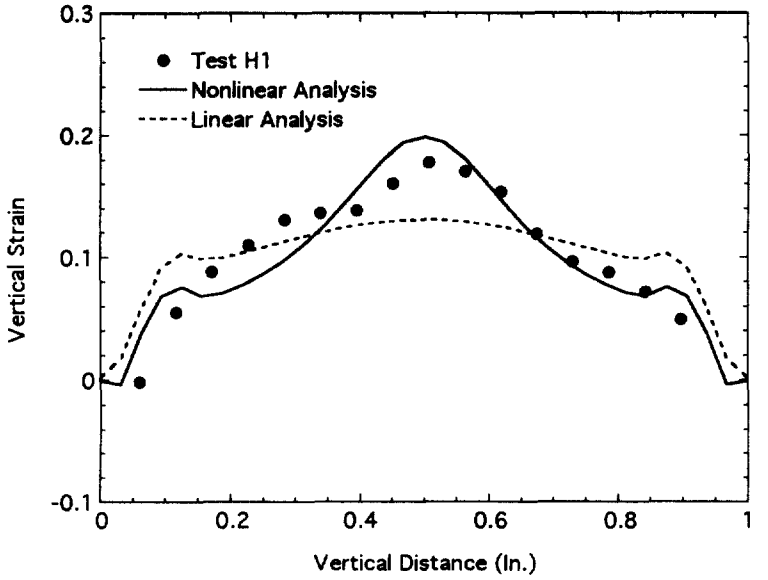

Fig. 14. Vertical strain comparison (10% global strain).

made from a left and right side vertical line cut through 0.05″ from hole edge, which is the closest line to the hole for the available strain data. It shows a clear distinction between the predictions from the linear model and the nonlinear model. Also, the experimental results are located closer to nonlinear predictions than linear predictions. The discrepancy between experiment and nonlinear theory at the 0.5″ position may be due in part to an experimental factor, i.e. the data smoothing; note also that the strain is well above that used in the characterization, as may be seen in Fig. 1. In Figure 16 the vertical strain predictions are compared to the experimental results along the cut through vertical lines at 0.17″ distance from both crack tips. Both linear and nonlinear predictions give good agreement with experiments; but it appears that the nonlinear prediction of maximum strain is at least slightly better than the linear prediction.

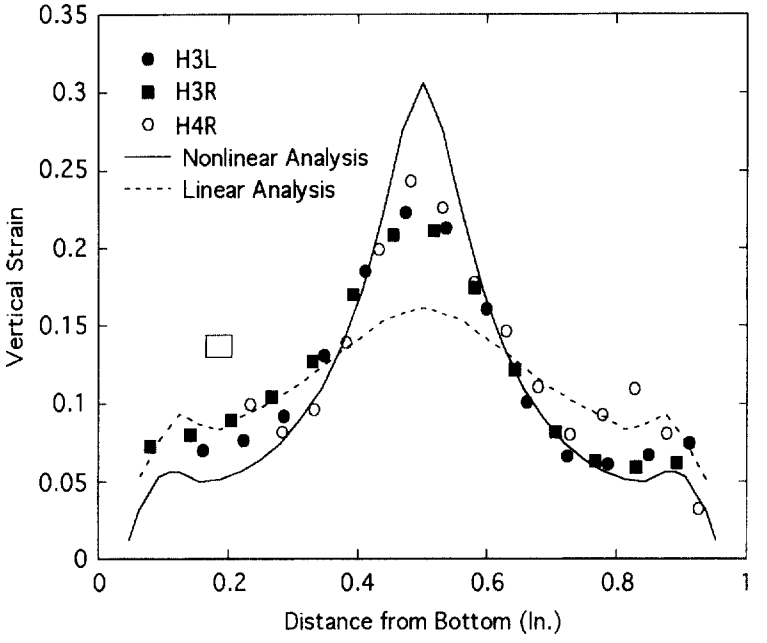

Fig. 15. Vertical strain comparisons for specimens with a hole (10% global strain).

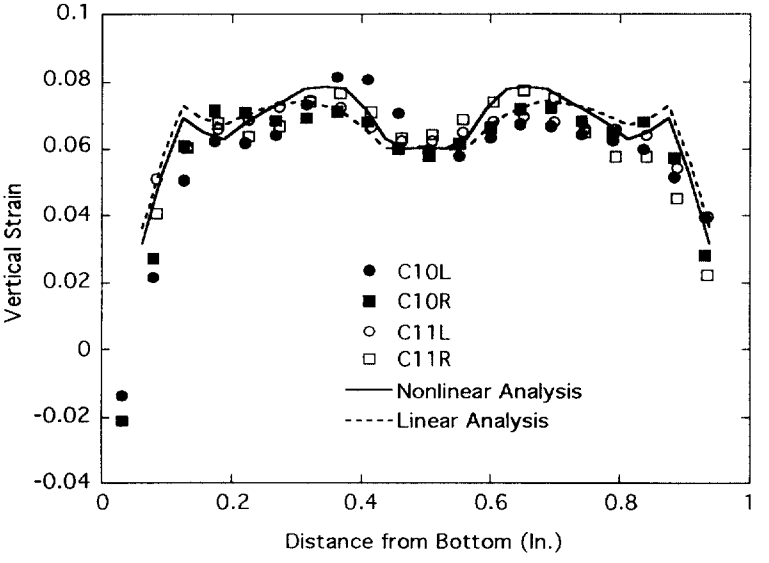

Fig. 16. Vertical strain comparisons for specimens with a crack (6% global strain).

4.3. *The effect of geometric nonlinearity*

The constitutive equation used so far has been expressed in terms of pseudo strains and displacements, and the problems we solved at a fixed time were elastic problems with rate-dependent damage. There was no approximation in the conversion of the elastic solution to the viscoelastic solution using the correspondence principle (Schapery, 1984). Since this constitutive relation is based on data from an axially symmetric loading which covered the primary strain ranges in the current experiments, the predictions should not have significant error due to geometric nonlinearities if the local rotations are small when displacement gradient is adopted for strain measure (Schapery, 1984). On the other hand, the use of Green's strain measure can fully take care of finite strain and rotation effects, but it creates error in the correspondence principle.

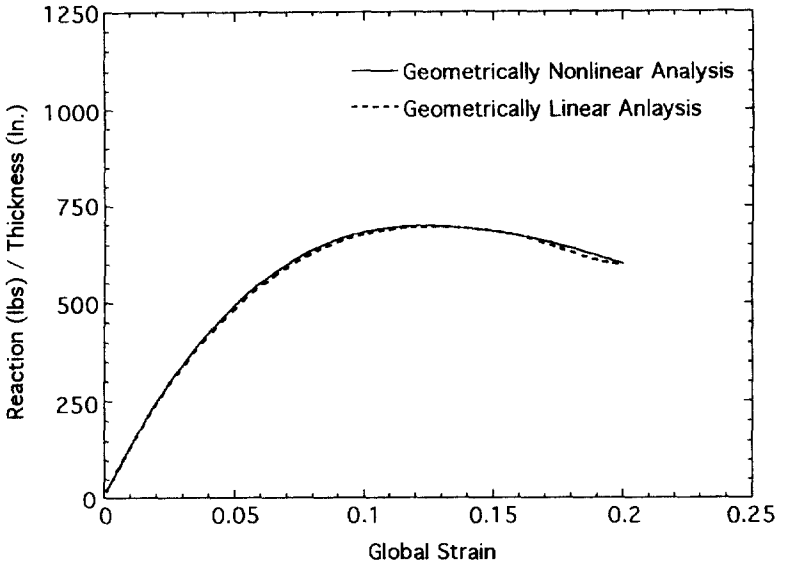

Fig. 17. Reaction comparison for a specimen without a crack ($\dot{\varepsilon} = 0.1\ \text{min}^{-1}$, $t = 0.2''$, $h = 1.0''$).

To see if there is much geometrically nonlinear effect on the previous analysis, including rigid body rotation effects, a few geometrically nonlinear analyses were performed and the results were compared to those from geometrically linear analysis (Ha, 1996). As far as strains are concerned, the pseudo strain distributions from the previous analysis are considered to be those from an elastic analysis, but the internal state changes according to the damage evolution laws. The following study is concerned with the geometrically nonlinear effect on the reaction load in an elasticity problem; i.e. we consider the pseudo strain to be physical strain. For specimens with and without a crack, the three-dimensional nonlinear elastic constitutive relation which allows finite strains and rigid body rotations with damage growth was formulated and computer-programmed.

Let us introduce Green's strain as,

$$\varepsilon^g = \tfrac{1}{2}(\mathbf{F}^T\mathbf{F} - \mathbf{I}). \tag{19}$$

where $\mathbf{F}$ is the deformation gradient tensor and $\mathbf{I}$ is identity tensor. The strain energy function in (15) can be rewritten in terms of principal Green's strains using the relations between principal Green's strains and engineering strains (displacement gradients) ε_p,

$$\varepsilon_p = \sqrt{1+2\varepsilon_p^g} - 1. \tag{20}$$

Next, principal second Piola–Kirchhoff stresses S_p can be derived from

$$S_p = \frac{\partial W^R}{\partial \varepsilon_p^g}. \tag{21}$$

Figures 17 and 18 give the comparison of loads in the geometrically nonlinear and linear analysis for a specimen without and with a one-inch center-through crack, respectively. The maximum discrepancy in the reaction force is about 0.3 and 1.5%, respectively.

The experimental strain field provides a similar conclusion. For example, the initiation of macrocrack growth in an initially cracked specimen started at relatively low global strain, less than 8%. By inspection of scanned images at 8 and 10% global strain, the crack tip opening angle retained almost the same low angle (i.e., self-similar crack growth) during the continuation of the crack growth under 10% global strain. From the experimental

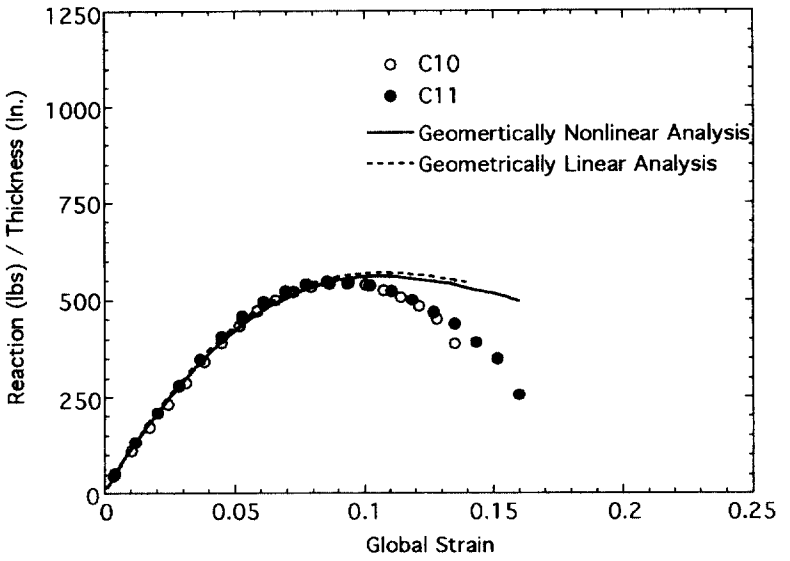

Fig. 18. Reaction comparison for a specimen with a crack ($\dot{\varepsilon} = 0.1$ min^{-1}, $t = 0.25''$ (I-Shape), $h = 1.0''$).

study on the local rigid body rotation of the material points on the C10 specimen surface, the only significant rigid body rotation was found to be limited to points very close to the wake region of the current crack tip, with a maximum rotation of less than 10°. Most other data points indicated less than 1° rotation.

The local strain distribution comparisons show very close agreement, with strains from geometrically linear analysis being slightly higher than those from geometrically nonlinear analysis (Ha, 1996). From a horizontal section plot along a line at 0.34″ distance from a crack in the unflawed body direction, the vertical strain difference was a maximum of about 3.7% of the strain itself. Thus, apart from points very close to crack tips or a hole (cf Fig. 15 at the center), it is concluded that there is little geometrically nonlinear effect in local strain distribution predictions for the specimens used in the test program of the current study.

5. CONCLUDING REMARKS

A nonlinear viscoelastic constitutive equation that is linear except for the effect of two internal state variables, was shown to successfully describe the viscoelastic behavior of a highly-filled, particulate composite with distributed damage using various biaxial strip geometries under constant applied displacement rate. Specifically, the constitutive equation was incorporated in a finite element model for analysis of these specimens. Both global reaction load and surface strain predictions from the nonlinear viscoelastic model provided good agreement with the experiments. The maximum load was predicted quite accurately for specimens without pre-cut cracks, after which macrocracking initiated; in this context, the theory is capable of predicting failure.

The three-dimensional nonlinear viscoelastic constitutive model can be conveniently employed in analysis of three-dimensional structures under monotonically increasing straining conditions. For unloading and reloading and for cyclic loading, an experimentally verified model exists that is based on pseudo strains, but it is presently limited to uniaxial loading (Schapery, 1982). The current numerical approach is limited to small rigid body rotation and small strain conditions. With finite strain effects, geometrically nonlinear analysis with elastic or quasi-elastic analysis and rate-dependent damage can be readily performed. The digital image correlation method we have used provides accurate surface strain fields for specimens of highly filled rubber under plane deformations. The present

version of this method may not give good results if there are large out-of-plane deformations (Post *et al.*, 1987), but it can be modified to account for them (Kahn-Zetter and Chu, 1990).

REFERENCES

Collingwood, G. A., Clark, L. M., Becker, J. D. and Becker, E. B. (1995) Evaluation of nonlinear viscoelastic constitutive theories by analyzing test specimens and instrumented subscale motors. *Proceedings of JANNAF Mechanical Behavior Working Group Meeting*, pp. 183–194. CPIA Pub 629.

Davis, I. L., (1994) Microstructural propellant constitutive theory: polymeric binder mechanical properties based on molecular structure. *Proceedings of JANNAF Mechanical Behavior Working Group Meeting*, pp. 239–253. CPIA Pub. 617.

Davis, D. D. (1995) Propellant aging/NDE feasibility study. *Proceedings of JANNAF Mechanical Behavior Working Group Meeting*, pp. 323–335. CPIA Pub. 629.

Dohrmann, C. R. and Busby, H. R. (1990) Spline function smoothing and differentiation of noisy data on a rectangular grid. *Proc. 1990 SEM Spring Conf. on Exp. Mech.*, 76–84.

Farris, R. J. (1968) The character of the stress–strain function for solid propellants. *Trans. Soc. Rheol.* **12,** 281–301.

Farris, R. J. *et al.* (1971) The stress–strain behavior of mechanically degradable polymers. *Polymer Networks: Structural and Mechanical Properties*, ed. A. J. Chompff and S. Newman. New York.

Farris, R. J. *et al.* (1975) Development of solid rocket propellant nonlinear viscoelastic constitutive theory. Air Force Rocket Propulsion Laboratory Report 75–20, May.

Gonzonas, G. A. (1993) A uniaxial nonlinear viscoelastic constitutive model with damage for M30 gun propellant. *Mechanics of Materials*, **15,** 323–335.

Ha, K. (1996) Evaluation of a three-dimensional, viscoelastic constitutive model for filled elastomers with distributed damage. Ph.D. dissertation, ASE/EM Department, The University of Texas at Austin.

Hibbit, Karlsson and Sorenson Inc. (1992) *ABAQUS User's Manual*, Vol. II, Version 5.2. Hibbit, Karlsson and Sorenson Inc.

Hibbit, Karlsson and Sorenson Inc. (1993) *ABAQUS Theory*, Version 5.3. Hibbit, Karlsson and Sorenson Inc., Section 2.3.

Hufferd, W. L. (1980) Thermal–mechanical interaction in filled polymers. *Proceedings of the NSF Workshop on a Continuum Mechanics Approach to Damage and Life Prediction.* Carrollton, Ky.

Kahn-Zetter, Z. L. and Chu, T. C. (1990) Three-dimensional displacement measurements using digital image correlation and photogrammic analysis. *Experimental Mechanics* **30**(2), 10–16.

Laheru, K. L. (1995) Piecewise-in-time linear elastic model for nonlinear viscoelastic materials. *Proceedings of JANNAF Mechanical Behavior Working Group Meeting*, pp. 217–228. CPIA Pub 629.

Lai, J. S. Y. and Findley, W. N. (1973) Creep of polyurethane under varying temperature for nonlinear uniaxial stress. *Transactions of the Society of Rheology* **17,** 63–87.

Mullins, L. (1969) Softening of rubber by deformation. *Rubber Chem. and Technology* **42,** 339–362.

Ozupek, S. and Becker, E. B. (1992) Constitutive modeling of high-elongation solid propellants. *Journal of Engineering Materials and Technology* **114,** 111–115.

Park, S. W. (1994) Development of a nonlinear thermo-viscoelastic constitutive equation for particulate composites with damage. Ph.D. dissertation, ASE/EM Department, The University of Texas at Austin.

Park, S. W. and Schapery, R. A. (1997) A viscoelastic constitutive model for particulate composites with growing damage. *International Journal of Solids and Structures* **34,** 931–947.

Park, S. W., Kim, Y. R. and Schapery, R. A. (1996) A viscoelastic continuum damage model and its application to uniaxial behavior of asphalt concrete. *Mechanics of Materials* **24,** 241–255.

Peng, T. J. (1993a) Constitutive equations of solid propellants with volume dilatation under multiaxial loading—Part 1 theory of dilatation and dewetting criterion. *Proceedings of JANNAF Mechanical Behavior Working Group Meeting*, pp. 159–176. CPIA Pub. 604.

Peng, T. J. (1993b) Constitutive equations of solid propellants with volume dilatation under multiaxial loading—Part 2 determination of the shear part of the potential function in terms of volume-preserved principal stretch ratios. *Proceedings of JANNAF Mechanical Behavior Working Group Meeting*, pp. 177–196. CPIA Pub. 604.

Post, D., Smith, C. and Czaneck, R. (1987) Crack opening and extension in inert solid propellant. Final Report AFRPL TR-87-043. Virginia Polytechnic Institute and State University.

Schapery, R. A. (1974) A nonlinear constitutive theory for particulate composites based on viscoelastic fracture mechanics. *Proceedings of JANNAF Mechanical Behavior Working Group Meeting*, pp. 313–328. CPIA Pub. 253.

Schapery, R. A. (1981) On viscoelastic deformation and failure behavior of composite materials with distributed flaws. In *Advances in Aerospace Structures and Materials*, ed. S. S. Wang and W. J. Renton, pp. 5–20. ASME, Vol. AD-01.

Schapery, R. A. (1982) Models for damage growth and fracture in nonlinear viscoelastic particulate composites. *Proceedings of the Ninth U.S. National Congress of Applied Mechanics*, Book H00228, pp. 237–245. ASME.

Schapery, R. A. (1984) Correspondence principles and a generalized *J*-integral for large deformation and fracture analysis of viscoelastic media. *International Journal of Fracture* **25,** 195–223.

Schapery, R. A. (1986) A micromechanical model for nonlinear viscoelastic behavior of particle-reinforced rubber with distributed damage. *Engineering Fracture Mechanics* **25,** 845–867.

Schapery, R. A. (1987) Nonlinear constitutive equations for solid propellant based on a work potential and micromechanical model. *Proceedings of JANNAF Mechanical Behavior Working Group Meeting.* CPIA, Pub., Baltimore, MD.

Schapery, R. A. (1991) Analysis of damage growth in particulate composites using a work potential. *Composites Engineering* **1**(3), 167–182.

Simo, J. C. (1987) On a fully three-dimensional finite-strain viscoelastic damage model: formulation and computational aspects. *Computer Methods in App. Mech. and Engrng* **60,** 153–173.

Springfield, C. W., McLeod, M. P. and Berry, D. M. (1993) A large strain constitutive law for finite element analysis of RSRM propellant. *Proceedings of JANNAF Mechanical Behavior Working Group Meeting*, pp. 293–305. CPIA Pub. 604.

Swanson, S. R. and Christensen, L. W. (1983) A constitutive formulation for high-elongation propellants. *J. Spacecraft* **20,** 559–566.

Whaba, G. (1975) Smoothing noisy data with spline functions. *Numer. Math.* **24,** 383–393.

Zhou, Jianping (1993) A constitutive model of polymer materials including chemical aging and mechanical damage and its experimental verification. *Polymer* **34,** 4252–4256.